

Observation of momentum-dependent charge density wave gap in a layered antiferromagnet GdTe_3

Sabin Regmi^{1,6}, Iftakhar Bin Elius¹, Anup Pradhan Sakhya¹, Dylan Jeff^{1,2}, Milo Sprague¹, Mazharul Islam Mondal¹, Damani Jarrett¹, Nathan Valadez¹, Alexis Agosto¹, Tetiana Romanova³, Jiun-Haw Chu⁴, Saiful I. Khondaker^{1,2}, Andrzej Ptok⁵, Dariusz Kaczorowski³, Madhab Neupane^{*1}

¹*Department of Physics, University of Central Florida, Orlando, Florida 32816, USA*

²*NanoScience Technology Center, University of Central Florida, Orlando, Florida 32826, USA*

³*Institute of Low Temperature and Structure Research, Polish Academy of Sciences, Okólna 2, PL-50-422 Wrocław, Poland*

⁴*Department of Physics, University of Washington, Seattle, Washington 98195, USA*

⁵*Institute of Nuclear Physics, Polish Academy of Sciences, W. E. Radzikowskiego 152, PL-31342 Kraków, Poland*

⁶*Present address: Center for Quantum Actinide Science and Technology, Idaho National laboratory, Idaho Falls, ID 83415, USA*

*Corresponding author: madhab.neupane@ucf.edu

Charge density wave (CDW) ordering has been an important topic of study for a long time owing to its connection with other exotic phases such as superconductivity and magnetism. The $R\text{Te}_3$ ($R =$ rare-earth elements) family of materials provides a fertile ground to study the dynamics of CDW in van der Waals layered materials, and the presence of magnetism in these materials allows to explore the interplay among CDW and long range magnetic ordering. Here, we have carried out a high-resolution angle-resolved photoemission spectroscopy (ARPES) study of a CDW material GdTe_3 , which is antiferromagnetic below ~ 12 K, along with thermodynamic, electrical transport, magnetic, and Raman measurements. Our ARPES data show a two-fold symmetric Fermi surface with both gapped and ungapped regions indicative of the partial nesting. The gap is momentum dependent, maximum along $\bar{\Gamma} - \bar{Z}$ and gradually decreases going towards $\bar{\Gamma} - \bar{X}$. Our study provides a platform to study the dynamics of CDW and its interaction with other physical orders in two- and three-dimensions.

Charge density wave (CDW) [1, 2] in quantum materials have been a subject of numerous research works for a number of decades because of its relevance in understanding several physical properties and also its competition or coexistence with exotic phases like superconductivity and magnetism [3–14]. CDW ordering is a phenomenon associated with Fermi surface (FS) instabilities, where a periodic lattice distortion leads to the spatial modulation of carrier density [2]. One example is the Peierls distortion in one-dimension [15, 16], in which the lattice periodicity can be doubled by electronically disturbing the system with a wave vector that is double the Fermi wave number, resulting into a gap opening at the Brillouin zone (BZ) boundaries nested by the same wave vector (FS nesting). With increase in dimensions, the FS nesting tends to be imperfect so that certain regions of the FS remain ungapped, leading to a metallic nature [17, 18]. The mechanism of CDW in such higher-dimensional materials is still of great interest as it can differ from material to material, can have different origin, and also depends on crystal growth conditions [19–22].

The orthorhombic crystalline family of van der Waals layered materials $R\text{Te}_3$ ($R =$ rare-earth elements) has been broadly studied for the presence of CDW [23–27]. The CDW

ordering takes place at a high temperature, and materials with heavier rare-earth elements exhibit a second CDW transition at a lower temperature [28, 29]. In addition, the existence of long range magnetic ordering in these compounds provides ground to study the interplay among magnetic and CDW orders [30, 31]. $R - \text{Te}$ slabs are sandwiched in between planar bi-layers of $\text{Te} - \text{Te}$, where the neighboring $\text{Te} - \text{Te}$ are connected through weak van der Waals interaction, thereby easing the exfoliation of these layered materials to the two-dimensional limit [32–35]. Angle-resolved photoemission spectroscopy (ARPES) [36, 37] has been a useful tool to directly probe the energy-momentum dispersion in quantum materials. It has been extensively used to study the electronic structure of $R\text{Te}_3$ in the investigation of FS and CDW induced gap [17, 38–47]. The gap size is found to depend on momentum, and the maximum gap changes as a function of the rare-earth element R , which can be modeled by a nesting driven sinusoidal CDW [40]. Among the materials under this family, GdTe_3 has been reported to have very high electronic mobility [33] and steep band dispersion at the Fermi level [45]. It can be thinned down to ultrathin limit using mechanical exfoliation that allows to study the thickness dependence of the CDW ordering [32, 33]. Properties such as CDW ordering, magnetic ordering, and pressure induced superconductivity [28, 31, 48] make this system interesting in order to explore more on the electronic properties.

In this article, by utilizing high-resolution ARPES measurements, we study the electronic structure of layered van der Waals material GdTe_3 . Our thermodynamic and electrical transport measurements show that the material is antiferromagnetic (AFM), with the magnetic transition occurring below ~ 12 K. The CDW transition occurs well above room temperature, at around ~ 375 K. Our ARPES results show two-fold symmetric FS with spectral intensity absent around certain regions of the FS, especially around $\bar{\Gamma} - \bar{\text{M}}$ to $\bar{\Gamma} - \bar{\text{Z}}$, indicating the presence of gap at the Fermi level. Some regions of the FS near the $\bar{\text{X}}$ point remain gapless, implying partial nesting. This gap is strongly direction dependent, with a gap maximum along $\bar{\Gamma} - \bar{\text{Z}}$ and gradually decreasing towards $\bar{\Gamma} - \bar{\text{X}}$. The room temperature Raman spectroscopy measurement shows the presence of CDW amplitude mode in the bulk as well as ultrathin samples up to 4L (~ 5 nm). Our results indicate that this material is excellent for studying the dynamics and interaction of CDW with other physical parameters in both three- and two-dimensional limits.

High-quality single crystals of GdTe_3 were synthesized using the self-flux technique, as described in the literature [52]. Chemical composition and phase homogeneity of the crystals were determined by means of energy-dispersive x-ray (EDX) analysis performed using a FEI scanning electron microscope equipped with an EDAX Genesis XM4 spectrometer. The specimens examined were found homogeneous and single-phase. The crystal structure was verified by powder x-ray diffraction (XRD) made on finely pulverized crystals employing a PANalytical X'pert Pro diffractometer with Cu K_α radiation. The XRD data was evaluated using the Rietveld method and the FULLPROF software package. The result confirmed the orthorhombic structure (space group #63) and yielded the lattice parameters $a \approx c \approx 4.33 \text{ \AA}$, $b = 25.3 \text{ \AA}$. In addition, the single crystal selected for physical properties measurements was examined on an Oxford Diffraction X'calibur four-circle single-crystal x-ray diffractometer equipped with a CCD Atlas detector.

Magnetic properties were investigated from 1.72 K to 300 K and in magnetic fields up to 7 T, applied perpendicular to the crystallographic b -axis, using a Quantum Design MPMS-XL superconducting quantum interference device (SQUID) magnetometer. The heat capacity was measured in the temperature interval 2 – 400 K employing the relaxation technique and two- τ model implemented in a Quantum Design PPMS-9 platform. Electrical transport measurements were performed on a bar-shaped specimen cut from the oriented crystal using a wire saw. Electrical contacts were made by silver wires of diameter 20 μm , attached to the specimen's surface in a linear manner with a single-component silver paste. The experiments were carried out in the same PPMS platform in the temperature range 2 – 300 K employing a standard four-points ac technique and electrical current flowing within the crystallographic ac -plane.

Raman spectroscopy measurements were performed in ambient conditions using a Horiba LabRAM HR Evolution Spectrometer equipped with a 1,800 grooves/mm grating and a Synapse EMCCD detector. A frequency doubled Nd:YAG 532 nm excitation laser source was focused to a square micron sized beam spot using an 100x objective. An ultra-low-frequency (ULF) filter was utilized to resolve the CDW peak at low wavenumbers.

High-resolution ARPES measurements were performed at the Stanford Synchrotron Radiation Lightsource (SSRL) end-station 5-2 equipped with a DA30 electron analyzer. The angular and energy resolutions were set better than 0.2° and 20 meV, respectively. The samples, mounted on copper posts and attached to ceramic posts on top using silver epoxy

paste, were loaded and cleaved *in situ* inside the ARPES chamber maintained under ultra high vacuum better than 10^{-10} torr. Measurements were carried out at a temperature of 8 K. The Fermi level was determined by fitting the leading edge in the energy distribution curve of gold spectrum, and the gap was obtained by fitting the leading edge of the energy distribution curves (EDCs) and comparing the shift from the so-determined Fermi level.

The first-principles calculations based on density-functional theory (DFT) [53, 54] were performed using the projector augmented-wave (PAW) potentials [55] implemented in the QUANTUM ESPRESSO [56–58]. The calculations were performed within the generalized gradient approximation (GGA) in the Perdew, Burke, and Ernzerhof (PBE) parameterization [59], develop within PSLIBRARY [60]. The atom position was optimized for conventional unit cell with experimental values of lattice vectors, using the $14 \times 2 \times 14$ \mathbf{k} -point grid in the Monkhorst–Pack scheme [61]. As the convergence condition for the optimization loop, we took the energy difference of 10^{-6} eV. The calculations were performed with the energy cut-off set to 400 eV. In calculations, the Gd $4f$ electrons were treated as valence states. To theoretical study of electronic band structure, we use the tight binding model in the maximally localized Wannier orbitals basis [62, 63]. This model was constructed from exact DFT calculations in a conventional unit cell, with $6 \times 2 \times 6$ Γ -centered \mathbf{k} -point grid, using the WANNIER90 software [64]. The tight binding (28 orbitals 112 bands) model is based on d orbitals of Gd, and p orbitals of Te. Finally, the spectrum of the system were calculated using the surface Green’s function technique for a semi-infinite system [65], implemented in WannierTools [66].

GdTe₃ crystallizes in a layered orthorhombic structure (space group Number 63) with lattice parameters $a \approx c \approx 4.33$ Å and $b = 25.28$ Å, close to the values reported in literature [33]. In Figure 1a, we present the side view of the crystal structure of GdTe₃, where pink balls represent the gadolinium atoms and teal colored balls represent the tellurium atoms. The crystal structure is composed of Gd – Te slabs sandwiched in between the Te bi-layers. Neighboring Te layers are bonded by weak van der Waals interaction, and the natural cleaving plane is parallel to the ac plane - the (010) plane. In Figure 1b, we show the spectroscopic core level spectrum, where peaks associated with Te $4d$ and Gd $4f$ can be clearly identified.

GdTe₃ exhibits a CDW phase transition, with the transition temperature well above room temperature (~ 377 K) [28]. In addition, it also undergoes an AFM transition at a

low temperature of ~ 12 K [31, 33, 49]. Our heat capacity (C) measurements also show an anomaly near 375 K (see Supplementary Note 1 & Supplementary Figure 1) that arises due to the incommensurate charge density wave formation [27]. The room temperature Raman spectrum for the bulk crystal shows a CDW amplitude mode along with other phonon modes, in concert with the literature [32, 51], establishing the presence of room-temperature CDW in the material. The mode remains prominent when the bulk crystal is thinned down to 4-layered samples via gold-assisted mechanical exfoliation, which suggests this material to be an excellent platform to study the interplay of CDW and long-range orders down to the two-dimensional limit as well [see Supplementary Note 2 & Supplementary Figure 2]. Figure 1c displays the temperature dependence of the electrical resistivity (ρ) of GdTe₃ measured with electrical current flowing in the crystallographic ac -plane. In concert with the previous reports [28, 31, 33], single crystals of GdTe₃ investigated in the present study exhibit very good metallic-type charge conductance. The ratio of the resistivity values measured at 300 K and 2 K is as large as 140, thus indicating high crystalline quality of the samples. On approaching the room temperature, the $\rho(T)$ curve clearly changes its slope signaling the proximity of the CDW transition. Figure 1d displays the temperature dependence of the inverse magnetic susceptibility (χ^{-1}) measured for magnetic field applied perpendicular to the crystallographic b -axis. Above about 30 K, $\chi^{-1}(T)$ exhibits a straight line behavior that can be approximated by the Curie-Weiss formula with the effective magnetic moment $\mu_{eff} = 7.67 \mu_B$ and the paramagnetic Curie temperature $\theta_p = -12.6$ K. The value of μ_{eff} is close to the theoretical prediction for Gd³⁺ ion. The negative value of θ_p reflects the predominance of AFM exchange interactions, which bring about the long range AFM ordering below about 12 K (see the upper inset to Figure 1d). The AFM nature of the electronic ground state in GdTe₃ is further corroborated by the characteristic behavior of the magnetization isotherm taken at $T = 1.72$ K (see the lower inset in Figure 1d) with a clear metamagnetic transition near 1.5 T. Overall, the magnetic data collected in our study agrees very well with those reported in the literature [30, 33, 49]. We also observed a distinct lambda-shaped anomaly at around 11.6 K in $C(T)$ graph, followed by a subsequent feature observed at 10 K (Figure 1e), similar to previous reports [31, 33, 49].

In Figure 1e, we present a schematic of the non-CDW FS of RTe₃. The bands crossing the Fermi level come from the p orbitals of the atoms within the Te layers. The two-dimensional

unfolded band structure (dark green bands referred to as main bands hereafter) corresponds to "true" square lattice with one Te atom in the primitive unit cell. Such unit cell can be obtained by $\sqrt{2}$ times reduction and 45° rotation of the unit cell of the whole crystal structure. To account for the three-dimensional lattice symmetry, the FS is acquired by considering the folding of the bands in the Te plane leading to the folded BZ represented by the red square in Figure 1e. The band folding is reflected on the observed band structure, where the mismatch between bands lead to their occurrence as the low intensity shadow bands [40, 42]. In Figure 1e, $q = \frac{5}{7}c^*$ represents a nesting condition, where the wave vector nests two sets of the main bands, which would still be present if we only consider the two-dimensional unit cell of the Te plane without folding.

The constant energy contours obtained at the FS and at various binding energies using a photon source of energy 90 eV ($T = 8$ K) are presented in Figure 2. The BZ represented by the dashed red lines is obtained from the (010) surface projection of the three-dimensional BZ. As seen in Figure 2a, the FS is metallic, in agreement with the metallic nature observed in the transport measurements, and is two-fold symmetric. Strong photoemission intensity is observed at the Fermi level along and around the $\bar{\Gamma} - \bar{X}$ direction. However, the intensity for the main bands along the $\bar{\Gamma} - \bar{M}$ and $\bar{\Gamma} - \bar{Z}$ directions is missing. On going to lower binding energy of about 100 meV, the intensity of the main bands starts to fill up towards the $\bar{\Gamma} - \bar{M}$ line, however, a gap still exists along the $\bar{\Gamma} - \bar{M}$ and $\bar{\Gamma} - \bar{Z}$ directions. The main band intensity only fills up along the $\bar{\Gamma} - \bar{M}$ line at around ~ 140 meV binding energy and along the $\bar{\Gamma} - \bar{Z}$ line at ~ 310 meV binding energy. These results indicate that a gap exists at the Fermi level along the $\bar{\Gamma} - \bar{M}$ and $\bar{\Gamma} - \bar{Z}$ directions. Similar nature of the gap was obtained in different set of measurements performed using 68 eV incident photon energy, in which the main band intensity appears along the $\bar{\Gamma} - \bar{M}$ and $\bar{\Gamma} - \bar{Z}$ directions, only around the binding energies of ~ 150 meV and ~ 320 meV binding energies, respectively [see Supplementary Note 3 & Supplementary Figure 3]. In Figure 2h, we present the theoretically calculated FS (without considering CDW), which is similar to the one presented in Figure 1e. To compare with the theoretical FS, we present the experimental energy contour in Figure 1e, which is integrated up to ~ 300 meV binding energy. Main bands as well as the shadow bands (from the folding), as previously described, can be observed. In addition to the low intensity bands coming from the folding of the three-dimensional BZ, we also observe other faint bands (shown by magenta colored arrows and traced by magenta colored curves) that

are not captured in the calculations [Also see Supplementary Note 4 and Supplementary Figure 4]. These bands arise as a result of the CDW ordering.

In order to quantify the gap along the $\bar{\Gamma} - \bar{M}$ and $\bar{\Gamma} - \bar{Z}$ directions, we took cuts along these directions and analyzed the corresponding band dispersion. In Figure 3a, we present the dispersion map along $\bar{\Gamma} - \bar{M}$ obtained using a photon source of 68 eV at a temperature of 8 K. From the band dispersion, there exists a gap along this direction line with the absence of photoemission signal in the FS. The second derivative plot of the band dispersion presented in Figure 3b shows that the bands extend up to the binding energy of about ~ 150 meV, and a clear gap exists above this binding energy along the $\bar{\Gamma} - \bar{M}$ direction. The gap of about 150 meV below the Fermi level can also be seen from the Fermi fit of the leading edge in the energy distribution curve (Figure 3c) taken within the momentum window represented by the magenta colored solid line in Figure 3a. Next, we turn our attention to explore the gap along $\bar{\Gamma} - \bar{Z}$. From the dispersion map (Figure 3d), its second derivative (Figure 3e), and the Fermi fit of the leading edge in energy distribution curve (Figure 3f), it is clear that a gap below the Fermi level of about ~ 320 meV exists along this direction. The dispersion maps for 90 eV incident photon energy are presented in the Supplementary Figure 5 [also see Supplementary Note 5], which show that gaps along the $\bar{\Gamma} - \bar{M}$ and $\bar{\Gamma} - \bar{Z}$ directions are ~ 140 meV and ~ 310 meV, respectively, as observed in the energy contours presented in Figure 2. The calculated band structures along these directions well reproduce the experimental data barring the CDW induced gap as the calculations are carried out for the non-CDW case. ARPES can only probe up to the Fermi energy, so the value of the total gap size can not be obtained from the ARPES measurements. Along $\bar{\Gamma} - \bar{X}$ and $\bar{M} - \bar{X}$, however, bands cross the Fermi level [Figure 3g,h; also see Supplementary Note 6 & supplementary Figure 6], which is in accordance with the photoemission intensity observed along this direction in the energy contours in Figure 2.

From the observations in Figures 2 and 3, we get the idea that the spectral intensity corresponding to the main bands appears at lower and lower binding energies as we move from $\bar{\Gamma} - \bar{X}$ to $\bar{\Gamma} - \bar{Z}$. In Figure 4, we analyze this momentum dependence of the gap below the Fermi level in measurements using a photon energy of 68 eV as a function of counter-clockwise angle from the $\bar{\Gamma} - \bar{Z}$ direction. 0° corresponds to the $\bar{\Gamma} - \bar{Z}$ direction and

a 45° counter-clockwise rotation means we are looking at the $\bar{\Gamma} - \bar{M}$ direction. Figure 4b represents the leading edges in the integrated energy distribution curves for dispersion maps corresponding to different angles defined in Figure 4a. It is clear that the leading edge shifts towards the Fermi level when we take the dispersion map away from the $\bar{\Gamma} - \bar{Z}$ direction towards the $\bar{\Gamma} - \bar{X}$ direction, indicative of reducing gap below the Fermi level. At an angle of 62°, the gap size surpasses the limits of the experimental energy resolution, therefore, it can be anticipated that the gap vanishes at greater angles [also see Supplementary Note 7 & Supplementary Figure 7]. In Figure 4c, we plot the gap below the Fermi level as a function of the counter-clockwise angle from $\bar{\Gamma} - \bar{Z}$, where with angle, the gap gradually reduces from around 320 meV at 0° to around 150 meV at 45°, i.e., $\bar{\Gamma} - \bar{M}$ direction and reaches out of experimental resolution at angles greater than 62°.

Given the existence of CDW ordering and AFM ordering in $R\text{Te}_3$ materials, in which 4*f* electrons coming from the *R*-element may bring electronic correlations into play, these materials are excellent platforms to study the interplay among electronic interactions, CDW, and long-range magnetic orders. The layered nature of the crystal structure with very weak van der Waals interaction provides opportunity to study such interplay in both three- and two-dimensions as mechanically exfoliating the crystals to the two-dimensional limit is easy. In this study, we studied bulk crystals of one of such materials GdTe_3 , which exhibits CDW transition at ~ 375 K and the magnetic ordering onsets below ~ 12 K [10, 28, 31, 33, 49]. The Gd 4*f* states are well below the Fermi level as seen in the spectroscopic core level measurement. We were able to obtain thin flakes of GdTe_3 via mechanical exfoliation, which still showed prominent CDW amplitude peak in the Raman spectrum taken at room temperature, indicating the presence of high-temperature CDW in the ultrathin limit as well. In fact, the CDW transition temperature is expected to increase with lowering of the sample thickness [32]. The FS obtained from ARPES measurement is two-fold symmetric. This two-fold symmetry instead of four-fold symmetry is as a result of slightly greater *c* than *a* ($c - a \sim 0.01$ Å [33]), and this changes possible two degenerate CDWs along *a* and *c* axes in favor of a single CDW along *c* direction with a CDW wave-vector $q_{CDW} = \frac{2}{7}c^*$ [23, 26, 28]. This wave vector connects the inner and outer diamond sheets in the FS, formed by the unfolded and folded band structures, respectively. An equivalent wave vector $q = c^* - q_{CDW} = \frac{5}{7}c^*$ nests the FS made by the main bands coming from a "true"

two-dimensional plane of Te atoms and therefore would be present even if the effects of the band folding scenario are not considered [28, 38, 50]. In our experimental data, the FS features coming from the shadow folded bands seem to be present even at the FS, however, the main band intensity is only along and around the $\bar{\Gamma} - \bar{X}$ direction and absent going away from this direction around $\bar{\Gamma} - \bar{M}$ and $\bar{\Gamma} - \bar{Z}$ directions. Therefore, our study shows that the CDW gap in GdTe₃ is governed by the nesting condition $q = \frac{5}{7}b^*$. Probing of the CDW gap is restricted to below the Fermi level, as the ARPES spectral function depends upon Fermi-Dirac function, which is zero above the Fermi energy. The gap below the Fermi level is strongly dependent on the direction along which we take the dispersion map - it is highest along $\bar{\Gamma} - \bar{Z}$ and reduces gradually towards $\bar{\Gamma} - \bar{X}$, vanishing before reaching $\bar{\Gamma} - \bar{X}$ line. Such a nature of the gap occurs in nesting driven CDW when the nesting is imperfect and has been reported in a previous study on RTe₃ which reports the nesting to become imperfect away from $k_x = 0$ [40]. Measurement performed at a different temperature of 15 K (conducted at a different beamline setup) reveals similar dependence on momentum (see Supplementary Figure 8). In addition to the CDW induced gap, we are able to identify some features that can not be described in the non-CDW FS with main and folded bands. These features also appear as shadow-like bands with weak intensity and are expected to originate due to the reconstruction caused by the CDW ordering.

To conclude, we studied a van der Waals layered material, GdTe₃, by performing high-resolution ARPES measurements of the electronic structure. We were able to probe the CDW induced gap as well as band features originating from the CDW ordering-induced reconstruction. The gap obtained in our study is strongly dependent on the momentum direction with the highest gap lying along the $\bar{\Gamma} - \bar{Z}$ direction. A prominent peak associated with the CDW amplitude mode is seen in our Raman measurements in samples as thin as 4L. Overall, our study demonstrates that GdTe₃ is an excellent material platform to investigate the dynamics of CDW and its connection with other physical orders like magnetism and superconductivity as a function of sample thickness ranging from three- to two-dimensions.

Acknowledgments - M.N. acknowledges the support from the National Science Foundation (NSF) CAREER award DMR-1847962, the NSF Partnerships for Research and Education in Materials (PREM) Grant DMR-2121953, and the Air Force Office of Scientific Research

MURI Grant No. FA9550-20-1-0322. D.K. was supported by the National Science Centre (Poland) under research grant 2021/41/B/ST3/01141. A.P. acknowledges the support by National Science Centre (NCN, Poland) under Projects No. 2021/43/B/ST3/02166 and also appreciates the funding in the frame of scholarships of the Minister of Science and Higher Education (Poland) for outstanding young scientists (2019 edition, No. 818/STYP/14/2019). S.I.K. acknowledges the support from the NSF PREM Grant DMR-2121953. The use of SSRL in SLAC National Accelerator Laboratory is supported by the U.S. Department of Energy (DOE), Office of Science, Office of Basic Energy Sciences under Contract No. DE-AC02-76SF00515. This research also used the resources of the Advanced Light Source (ALS), which is a DOE Office of Science User Facility under contract no. DE-AC02-05CH11231. We are grateful to Makoto Hashimoto & Donghui Lu at SSRL and Alexei Fedorov & Sung-Kwan Mo at ALS for the beamline assistance.

REFERENCES

- [1] Grüner, G. The dynamics of charge-density waves. *Rev. Mod. Phys.* **60**, 1129 (1988).
- [2] Grüner, G. *Density Waves In Solids* (Addison-Wesley, 1994).
- [3] Morris, R. C. Connection between Charge-Density Waves and Superconductivity in NbSe₂. *Phys. Rev. Lett.* **34**, 1164 (1975).
- [4] Gabovich, A. M. & Voitenko, A. I. Superconductors with charge- and spin-density waves: theory and experiment (Review). *Low Temp. Phys.* **26**, 305 (2000).
- [5] Jung, M. H., Ekino, T., Kwon, Y. S. & Takabatake, T. Tunneling spectroscopy of RTe₂ (R = La, Ce) and possible coexistence between charge-density waves and magnetic order. *Phys. Rev. B* **63**, 035101 (2000).
- [6] Gabovich, A. M., Voitenko, A. I., Annett, J. F. & Ausloos, M. Charge- and spin-density-wave superconductors. *Supercon. Sci. Technol.* **14**, R1 (2001).
- [7] Yokoya, T. et al. Fermi Surface Sheet-Dependent Superconductivity in 2H – NbSe₂. *Science* **294**, 2518 (2001).
- [8] Galli, F., et al. Coexistence of charge density wave and antiferromagnetism in Er₅Ir₄Si₁₀. *J. Phys. Condens. Matter* **14**, 5067 (2002).
- [9] Jung, M. H. et al. Superconductivity in magnetically ordered CeTe_{1.82}. *Phys. Rev. B* **67**, 212504 (2003).

- [10] Iyeiri, Y., Okumura, T., Michioka, C. & Suzuki, K. Magnetic properties of rare-earth metal tritellurides $R\text{Te}_3$ ($R = \text{Ce}, \text{Pr}, \text{Nd}, \text{Gd}, \text{Dy}$). *Phys. Rev. B* **67**, 144417 (2003).
- [11] Singh, Y., Nirmala, R., Ramakrishnan, S. & Malik, S. K. Competition between superconductivity and charge-density-wave ordering in the $\text{Lu}_5\text{Ir}_4(\text{Si}_{1-x}\text{Ge}_x)_{10}$ alloy system. *Phys. Rev. B* **72**, 045106 (2005).
- [12] Fang, L. et al. Competition of superconductivity and charge density wave order in Na_xTaS_2 single crystals. *Sci. Technol. Adv. Mater.* **6**, 736 (2005).
- [13] Hossain, Z. et al. Coexistence of magnetic order and charge density wave in a Kondo lattice: $\text{Yb}_5\text{Ir}_4\text{Si}_{10}$. *Phys. Rev. B* **71**, 060406 (2005).
- [14] Shimomura, S. et al. Charge-Density-Wave Destruction and Ferromagnetic Order in SmNiC_2 . *Phys. Rev. Lett.* **102**, 076404 (2009).
- [15] Peierls, R. & Peierls, R. E. *Quantum theory of solids* (Oxford University Press, 1955).
- [16] Ashcroft, N. W. & Mermin, N. D. *Solid State Physics* (Cengage Learning, 1976)
- [17] Gweon, G. H. et al. Direct Observation of Complete Fermi Surface, Imperfect Nesting, and Gap Anisotropy in the High-Temperature Incommensurate Charge-Density-Wave Compound SmTe_3 . *Phys. Rev. Lett.* **81**, 886 (1998).
- [18] Garcia, D. R. et al. Revealing Charge Density Wave Formation in the LaTe_2 System by Angle Resolved Photoemission Spectroscopy. *Phys. Rev. Lett.* **98**, 166403 (2007).
- [19] Johannes, M. D. & Mazin, I. I. Fermi surface nesting and the origin of charge density waves in metals. *Phys. Rev. B* **77**, 165135 (2008).
- [20] Zhu, X., Guo, J., Zhang, J. & Plummer, E. W. Misconceptions associated with the origin of charge density waves. *Adv. Phys. X* **2**, 622 (2017).
- [21] Thorne, R. E. Effect of crystal-growth conditions on charge-density-wave pinning in NbSe_3 . *Phys. Rev. B* **45**, 5804 (1992).
- [22] Sayers, C. J. et al. Correlation between crystal purity and the charge density wave in $1T-\text{VSe}_2$. *Phys. Rev. Mater.* **4**, 025002 (2020).
- [23] DiMasi, E., Aronson, M. C., Mansfield, J. F., Foran, B. & Lee, S. Chemical pressure and charge-density waves in rare-earth tritellurides. *Phys. Rev. B* **52**, 14516 (1995).
- [24] Laverock, J. et al. Fermi surface nesting and charge-density wave formation in rare-earth tritellurides. *Phys. Rev. B* **71**, 085114 (2005).
- [25] Malliakas, C., Billinge, S. J. L., Kim, H. J., & Kanatzidis, M. G. Square Nets of Tellurium:

- Rare-Earth Dependent Variation in the Charge-Density Wave of $RETe_3$ ($RE =$ Rare-Earth Element). *J. Am. Chem. Soc.* **127**, 6510 (2005).
- [26] Malliakas, C. & Kanatzidis M. G. Divergence in the Behavior of the Charge Density Wave in $RETe_3$ ($RE =$ Rare-Earth Element) with Temperature and RE Element. *J. Am. Chem. Soc.* **128**, 12612 (2006).
- [27] Yumigeta, K. et al. Advances in Rare-Earth Tritelluride Quantum Materials: Structure, Properties, and Synthesis. *Adv. Sci.* **8**, 2004762 (2021).
- [28] Ru, N. et al. Effect of chemical pressure on the charge density wave transition in rare-earth tritellurides RTe_3 . *Phys. Rev. B* **77**, 035114 (2008).
- [29] Banerjee, A. et al. Charge transfer and multiple density waves in the rare earth tellurides. *Phys. Rev. B* **87**, 155131 (2013).
- [30] Iyeiri, Y., Okumura, T., Michioka, C. & Suzuki, K. Magnetic properties of rare-earth metal tritellurides RTe_3 ($R =$ Ce, Pr, Nd, Gd, Dy). *Phys. Rev. B* **67**, 144417 (2003).
- [31] Ru, N. Chu, J. H., & Fisher, I. R. Magnetic properties of the charge density wave compounds RTe_3 ($R =$ Y, La, Ce, Pr, Nd, Sm, Gd, Tb, Dy, Ho, Er, and Tm). *Phys. Rev. B* **78**, 012410 (2008).
- [32] Chen, Y. et al. Raman spectra and dimensional effect on the charge density wave transition in $GdTe_3$. *Appl. Phys. Lett.* **115**, 151905 (2019).
- [33] Lei, S. et al. High mobility in a van der Waals layered antiferromagnetic metal. *Sci. Adv.* **6**, eaay6407 (2020).
- [34] Kogar, A. et al. Light-induced charge density wave in $LaTe_3$. *Nat. Phys.* **16**, 159 (2020).
- [35] Watanabe, M. et al. Shubnikov-de-Haas oscillation and possible modification of effective mass in $CeTe_3$ thin films. *AIP Adv.* **11**, 015005 (2021).
- [36] Damascelli, A., Hussain, Z. & Shen, Z.-X. Angle-resolved photoemission studies of the cuprate superconductors. *Rev. Mod. Phys.* **75**, 473 (2003).
- [37] Damascelli, A. Probing the Electronic Structure of Complex Systems by ARPES. *Phys. Scr.* **2004**, 61 (2004).
- [38] Brouet, V., et al. Fermi Surface Reconstruction in the CDW State of $CeTe_3$ Observed by Photoemission. *Phys. Rev. Lett.* **93**, 126405 (2004).
- [39] Komoda, H. et al. High-resolution angle-resolved photoemission study of incommensurate charge-density-wave compound $CeTe_3$. *Phys. Rev. B* **70**, 195101 (2004).

- [40] Brouet, V. et al. Angle-resolved photoemission study of the evolution of band structure and charge density wave properties in $R\text{Te}_3$ ($R = \text{Y}, \text{La}, \text{Ce}, \text{Sm}, \text{Gd}, \text{Tb}, \text{and Dy}$). *Phys. Rev. B* **77**, 235104 (2008).
- [41] Schmitt, F. et al. Transient Electronic Structure and Melting of a Charge Density Wave in TbTe_3 . *Science* **321**, 1649 (2008).
- [42] Moore, R. G. et al. Fermi surface evolution across multiple charge density wave transitions in ErTe_3 . *Phys. Rev. B* **81**, 073102 (2010).
- [43] Lou, R. et al. Interplay between multiple charge-density waves and the relationship with superconductivity in Pd_xHoTe_3 . *Phys. Rev. B* **93**, 115133 (2016).
- [44] Lee, E. et al. The 7×1 Fermi Surface Reconstruction in a Two-dimensional f-electron Charge Density Wave System: PrTe_3 . *Sci. Rep.* **6**, 30318 (2016).
- [45] Liu, J. S. et al. Electronic structure of the high-mobility two-dimensional antiferromagnetic metal GdTe_3 . *Phys. Rev. Materials* **4**, 114005 (2020).
- [46] Seong, S. et al. Angle-resolved photoemission spectroscopy study of a system with a double charge density wave transition: ErTe_3 . *Phys. Rev. B* **104**, 195153 (2021).
- [47] Chikina, A. et al. Charge density wave generated Fermi surfaces in NdTe_3 . *Phys. Rev. B* **107**, L161103 (2023).
- [48] Zocco, D. A. et al. Pressure dependence of the charge-density-wave and superconducting states in GdTe_3 , TbTe_3 , and DyTe_3 . *Phys. Rev. B* **91**, 205114 (2015).
- [49] Guo, Q., Bao, D., Zhao, L. J. & Ebisu, S. Novel magnetic behavior of antiferromagnetic GdTe_3 induced by magnetic field. *Physica B: Condensed Matter* **617**, 413153 (2021).
- [50] Fang, A., Ru, N., Fisher, I. R. & Kapitulnik, A. STM Studies of TbTe_3 : Evidence for a Fully Incommensurate Charge Density Wave. *Phys. Rev. Lett.* **99**, 046401 (2007).
- [51] Wang, Y. et al. Axial Higgs mode detected by quantum pathway interference in $R\text{Te}_3$. *Nature* **606**, 896 (2022).
- [52] Ru, N. & Fisher, I. R. Thermodynamic and transport properties of YTe_3 , LaTe_3 , and CeTe_3 . *Phys. Rev. B* **73**, 033101 (2006).
- [53] Hohenberg, P. & Kohn, W. Inhomogeneous Electron Gas. *Phys. Rev.* **136**, B864 (1964).
- [54] Kohn, W. & Sham, L. J. Self-Consistent Equations Including Exchange and Correlation Effects. *Phys. Rev.* **140**, A1133 (1965).

- [55] Blöchl, P. E. Projector augmented-wave method. *Phys. Rev. B* **50**, 17953 (1994).
- [56] Giannozzi, P. et al. QUANTUM ESPRESSO: a modular and open-source software project for quantum simulations of materials, *J. Phys. Condens. Matter* **21**, 395502 (2009).
- [57] Giannozzi, P. et al. Advanced capabilities for materials modelling with QUANTUM ESPRESSO. *J. Phys. Condens. Matter* **29**, 465901 (2017).
- [58] Giannozzi, P. et al. QUANTUM ESPRESSO toward the exascale. *J. Chem. Phys.* **152**, 154105 (2020).
- [59] Perdew, J. P., Burke, K. & Ernzerhof, M. Generalized Gradient Approximation Made Simple. *Phys. Rev. Lett.* **77**, 3865 (1996).
- [60] Dal Corso, A. Pseudopotentials periodic table: From H to Pu. *Comput. Mater. Sci.* **95**, 337 (2014).
- [61] Monkhorst, H. J. & Pack, J. D. Special points for Brillouin-zone integrations. *Phys. Rev. B* **13**, 5188 (1976).
- [62] Marzari, N. & Vanderbilt, D. Maximally localized generalized Wannier functions for composite energy bands. *Phys. Rev. B* **56**, 12847 (1997).
- [63] Souza, I., Marzari, N. & Vanderbilt, D. Maximally localized Wannier functions for entangled energy bands. *Phys. Rev. B* **65**, 035109 (2001).
- [64] Pizzi, G. et al. Wannier90 as a community code: new features and applications. *J. Phys. Condens. Matter* **32**, 165902 (2020).
- [65] Sancho, M. P. L., Sancho, J. M. L., Sancho, J. M. L. & Rubio, J. Highly convergent schemes for the calculation of bulk and surface Green functions. *J. Phys. F: Met. Phys.* **15**, 851 (1985).
- [66] Q. Wu, S. Zhang, H.-F. Song, M. Troyer, & A. A. Soluyanov, WannierTools: An open-source software package for novel topological materials, *Comput. Phys. Commun.* **224**, 405 (2018).

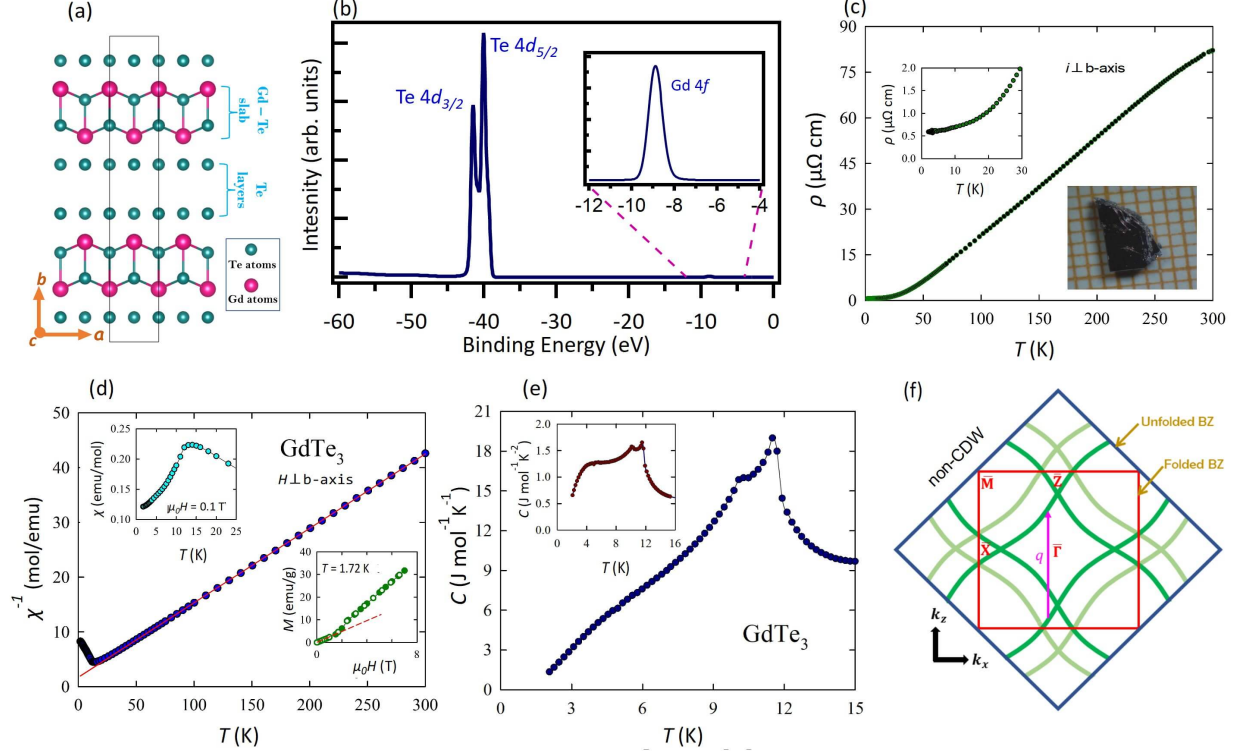


FIGURE 1. Crystal structure and sample characterization of GdTe_3 . **a** Crystal structure of GdTe_3 , where the pink and the teal colored balls represent Gd and Te atoms, respectively. **b** Spectroscopic core level spectrum showing peaks of Gd $4f$ and Te $4d$ peaks. **c** Temperature dependence of the electrical resistivity measured with electrical current flowing in the crystallographic $a - c$ plane. Inset: the low-temperature resistivity data. **d** Temperature variation of the inverse magnetic susceptibility measured in a magnetic field of 0.1 T applied perpendicular to the crystallographic b -axis. Solid line represents the Curie-Weiss fit described in the text. Top left inset: The low-temperature magnetic susceptibility data. Bottom right inset: Magnetic field variation of the magnetization taken at 1.72 K with increasing (full circles) and decreasing (open circles) field strength. Dashed line emphasizes a linear behavior in small fields and the metamagnetic transition near 1.5 T. **e** Low-temperature dependence of specific heat near the magnetic transition. Inset: Same data plotted as the ratio of specific heat to temperature versus temperature. **f** Schematic of non-CDW FS in $R\text{Te}_3$ showing two-dimensional BZ of Te plane and three-dimensional BZ from the three-dimensional unit cell.

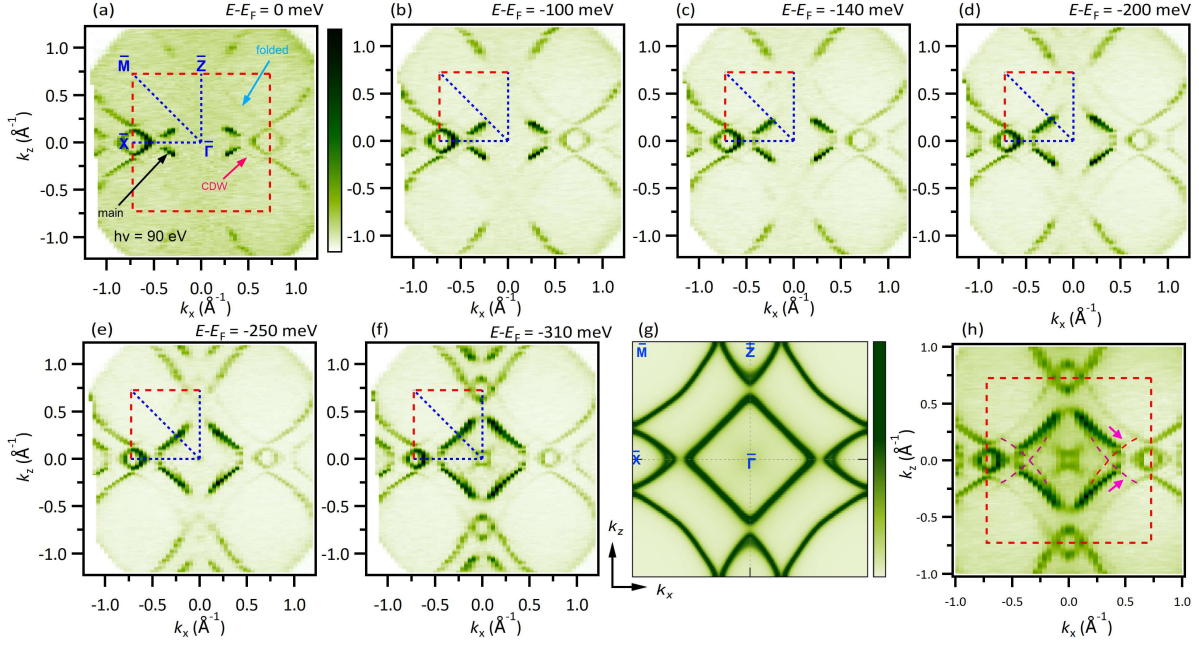


FIGURE 2. Constant energy contours on the (010) surface of GdTe_3 . **a** ARPES measured FS with a photon energy of 90 eV. Experimental BZ is shown with red dashed lines. High-symmetry points and directions are labeled in blue color. **b-f** Energy contours at various binding energies as noted on top of each plot. **g** Calculated FS for non-CDW case. **h** Energy contour integrated within 50 meV window centered at 300 meV binding energy. ARPES data were collected at the SSRL end-station 5-2 at a temperature of 8 K.

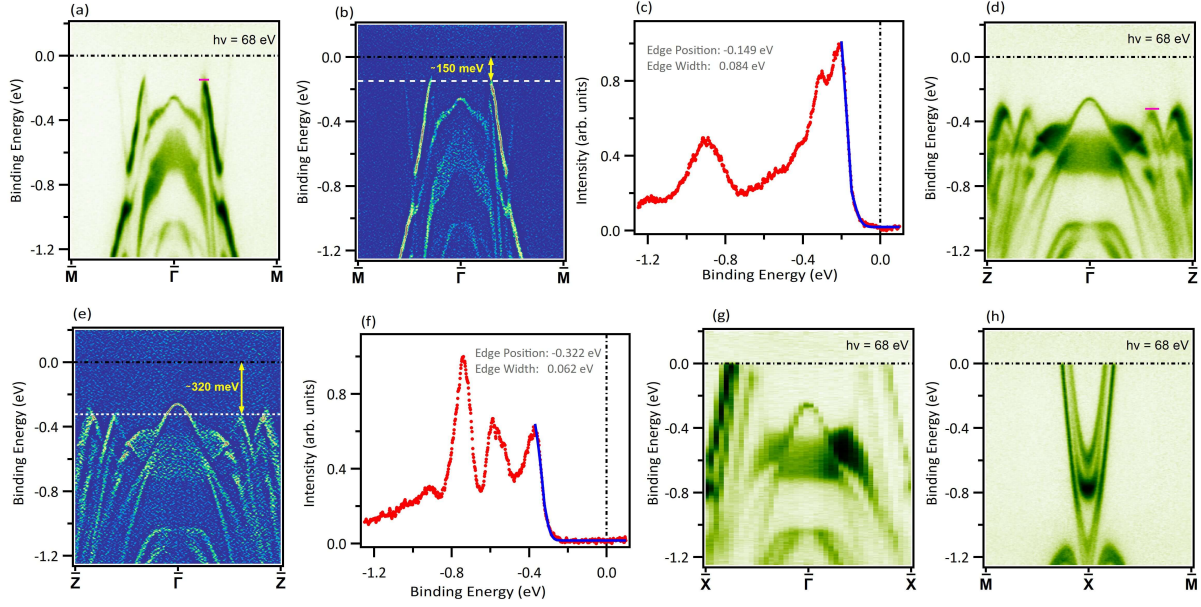


FIGURE 3. Experimental observation of CDW induced gap. **a** Dispersion map and **b** its second derivative along the $\bar{M} - \bar{\Gamma} - \bar{M}$ direction. **c** Energy distribution curve integrated within the momentum window represented by magenta line in (a) and the Fermi edge fit. **d** Dispersion map and **e** its second derivative along the $\bar{Z} - \bar{\Gamma} - \bar{Z}$ direction. **f** Energy distribution curve integrated within the momentum window represented by the magenta line in (d) and the Fermi edge fit. **g** Experimental dispersion map along the $\bar{X} - \bar{\Gamma} - \bar{X}$ direction. **h** Experimental band structure along $\bar{M} - \bar{X} - \bar{M}$. Data were collected at the SSRL beamline 5-2 at a temperature of 8 K.

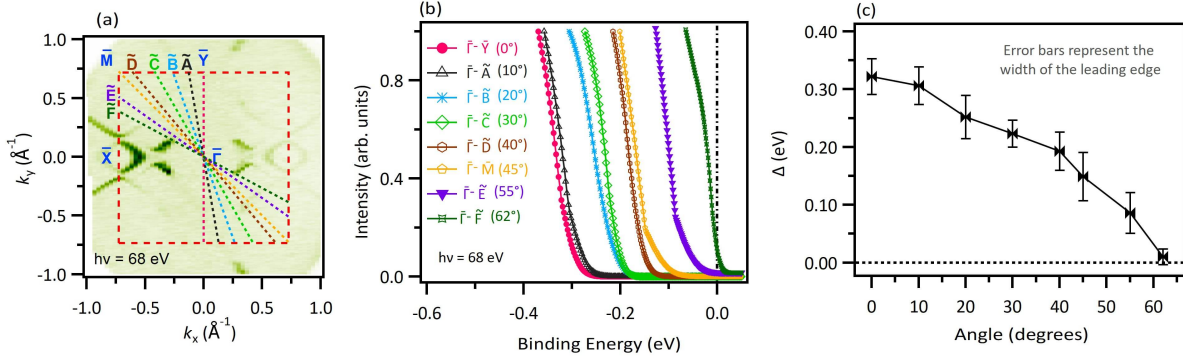


FIGURE 4. Momentum dependence of the gap. **a** FS measured with photon energy of 68 eV with colored lines representing the cuts at color-coded angles. The angles are taken with respect to the $\bar{Z} - \bar{\Gamma} - \bar{Z}$ direction. **b** Shift in the fitted Fermi edge on going away from $\bar{Z} - \bar{\Gamma} - \bar{Z}$. **c** Gap below the Fermi level plotted against the angle from the $\bar{Z} - \bar{\Gamma} - \bar{Z}$ direction. Data were collected at the SSRL beamline 5-2 at a temperature of 8 K.

SUPPLEMENTARY INFORMATION

SUPPLEMENTARY NOTE 1: SAMPLE CHARACTERIZATION AND HEAT CAPACITY MEASUREMENTS

High-quality single crystals of GdTe_3 were synthesized using the self-flux technique. Chemical composition and phase homogeneity of the crystals were determined by means of energy-dispersive X-ray (EDX) analysis performed using a FEI scanning electron microscope equipped with an EDAX Genesis XM4 spectrometer. The result of EDX analysis is presented in Supplementary Figure 1a, which indicates the desired stoichiometry and homogeneous chemical composition with 26.27 % Gd and 73.73 % Te. Supplementary Figure 1b shows the specific heat (C) of GdTe_3 measured up to 400 K, with inset showing a zoomed in view at high temperatures. Despite severe irregularities in the $C(T)$ curve caused by addenda contribution (Apiezon N grease), one can recognize an anomaly near 375 K that arises due to the incommensurate charge density wave formation [1].

SUPPLEMENTARY NOTE 2: RAMAN SPECTROSCOPY AND MECHANICAL EXFOLIATION OF THIN FLAKES

The exfoliation of the thin layer GdTe_3 samples was performed via Au-Assisted exfoliation. The metal layer deposition was completed in an electron/thermal evaporation system (Thermionics E-beam & RDM Thermal evaporator). A 2 nm metal adhesion layer of Ti was first evaporated onto a Si/SiO₂ substrate via e-beam evaporation. 5 nm of Au was then evaporated onto the Ti adhesion layer via thermal evaporation. Soon after exposing the Au layer to ambiance, the GdTe_3 crystals were cleaved from a parent crystal and lightly pressed onto the target substrate using Nitto tape (SPV-224 PVC) for one minute. Lifting the tape resulted in exfoliated thin layers of GdTe_3 on the Au/Ti/SiO₂/Si substrate.

Atomic force microscopy (AFM) was utilized to measure the thickness and identify the layer number of the exfoliated thin layer GdTe_3 . AFM measurements were taken in non-contact mode using a SmartSPM1000 scanning probe microscope. A single layer of GdTe_3 is reported to have a height of 1.2 nm, serving as the baseline for the measurement of the flake's layer number. The AFM measurements were taken in ambient conditions. Optical

image of representative thin flakes used in the Raman measurements are presented in Supplementary Figure 2a, where the arrow represents the location of where the Raman was measured. The AFM images are presented in Supplementary Figure 2b, with red line indicating the direction which height profile was taken. The height profile of corresponding thin flakes are presented in Supplementary Figure 2c.

In order to ensure that the Raman spectra being reported was of pristine conditions, the bulk GdTe_3 was cleaved before any Raman experimentation was done. The Raman spectra for bulk as well as for different layered samples up to 4L thin are presented in Supplementary Figure 2d. In the Raman spectrum, several peaks are observed, which is consistent with those reported in the literature [2, 3]. The peaks at 64 cm^{-1} and 79 cm^{-1} represent overlapping degenerate A_g and B_g phonon modes, the peak at 59 cm^{-1} is a two-fold symmetric phonon mode, the peaks at 104 cm^{-1} , 117 cm^{-1} , 129 cm^{-1} , 144 cm^{-1} are B_g symmetric phonons, and the peak at 91 cm^{-1} is an A_g symmetric phonon [3]. Of interest is the peak at 46 cm^{-1} , which has been reported to be the CDW amplitude mode [2, 3]. The presence of this strong peak at room temperature Raman data supports the presence of CDW phase at room temperature. In thin films up to 4L, this peak remains strong, indicative of the presence of room-temperature CDW in two-dimensional limit. In fact, it has been documented that the CDW transition shifts to higher temperature with diminishing thickness [2]. Thus, GdTe_3 could be an excellent platform for studying how different physical orders such as long-range magnetic, superconducting, charge-density wave, etc. in both three- and two-dimensions.

SUPPLEMENTARY NOTE 3: ARPES MEASURED CONSTANT ENERGY CONTOURS WITH PHOTON ENERGY OF 68 eV

In Supplementary Figure 3, we present the Fermi surface and constant energy contours measured with a photon energy of 68 eV obtained at 8 K. Similar to the observations in the main text Figure 2 (with 90 eV photon energy), the Fermi surface has some intensity along and around the $\bar{X}-\bar{\Gamma}-\bar{X}$ direction and no intensity along $\bar{M}-\bar{\Gamma}-\bar{M}$ and $\bar{Z}-\bar{\Gamma}-\bar{Z}$. Spectral intensity appears at $\sim 150 \text{ meV}$ binding energy along $\bar{M}-\bar{\Gamma}-\bar{M}$ and about $\sim 320 \text{ meV}$ binding energy along $\bar{Z}-\bar{\Gamma}-\bar{Z}$.

SUPPLEMENTARY NOTE 4: OBSERVATION OF CDW BANDS

In Supplementary Figure 4a, we present an integrated energy contour taken with 68 eV incident photon energy. The integration is done within a 50 meV window centered at the binding energy of 300 meV. Similar to the observation for 90 eV photon energy presented in the main text Figure 2h, the features that can not be described by the non-CDW calculations appear (shown by magenta colored arrow in 4a and represented by magenta colored dashed curves in 4b). An energy-momentum dispersion cut taken along the yellow colored dashed line in 4b at $k_x = -0.5 \text{ \AA}^{-1}$ is presented in Supplemental Figure 4c, where the intense main bands and shadow bands coming from both the band folding and CDW can be observed.

SUPPLEMENTARY NOTE 5: $\bar{M} - \bar{\Gamma} - \bar{M}$ AND $\bar{Z} - \bar{\Gamma} - \bar{Z}$ DISPERSION MAPS (90 eV)

In Supplementary Figure 5, we present the dispersion maps taken along the $\bar{M} - \bar{\Gamma} - \bar{M}$ and $\bar{Z} - \bar{\Gamma} - \bar{Z}$ directions taken from measurements using 90 eV photon energy. From the dispersion maps (5a and 5d) and their second derivative plots (5b and 5e), it is clear that the gap size below the Fermi level for 90 eV data are around 140 meV and 310 meV along $\bar{M} - \bar{\Gamma} - \bar{M}$ and $\bar{Z} - \bar{\Gamma} - \bar{Z}$, respectively in agreement with the observations in the constant energy contours presented in the main text Figure 2. In Supplementary Figures 5c and 5f, we present the theoretically calculated surface spectrum along the $\bar{M} - \bar{\Gamma} - \bar{M}$ and $\bar{Z} - \bar{\Gamma} - \bar{Z}$ directions, respectively. While the spectrum overall matches the experimental observation, the gap is not seen in the calculations as they are carried out for the non-CDW case.

SUPPLEMENTARY NOTE 6: DISPERSION MAPS ALONG $\bar{X} - \bar{\Gamma} - \bar{X}$ AND $\bar{M} - \bar{X} - \bar{M}$

Supplementary Figure 6(a) represents the dispersion map along the $\bar{\Gamma} - \bar{X}$ direction obtained from the measurement using a photon energy of 90 eV. Bands crossing the Fermi level can be clearly observed, indicative of the absence of gap along this direction. In Supplementary Figure 6(c), we show the dispersion map along the $\bar{M} - \bar{X}$ direction. Around

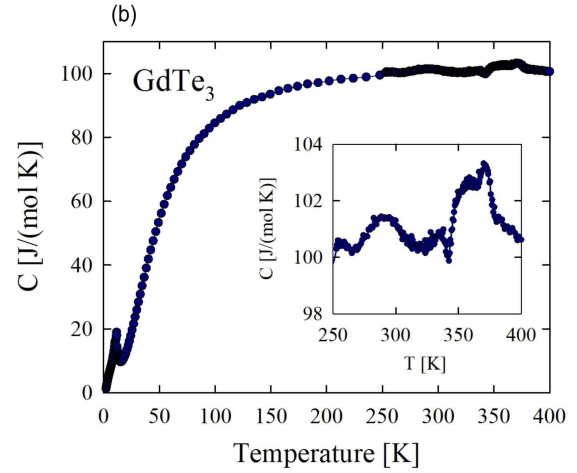
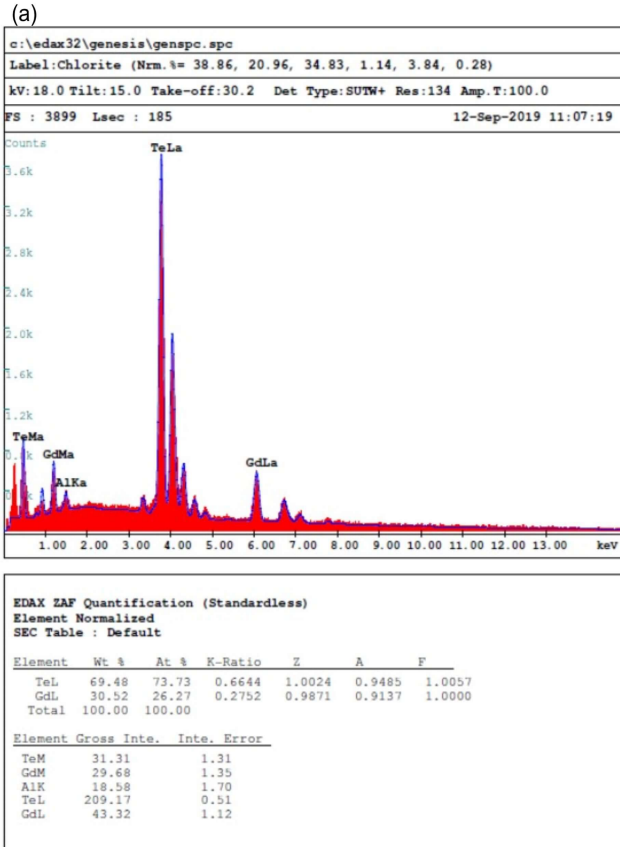
the \bar{X} point, bands are crossing the Fermi level, which again indicated the absence of any gap around the \bar{X} point as observed in the Fermi surface maps. The experimentally observed band dispersions along $\bar{\Gamma} - \bar{X}$ and $\bar{M} - \bar{X}$ are well reproduced in the theoretical surface spectrum calculated without considering CDW ordering [Figures 6b,d].

SUPPLEMENTARY NOTE 7: DIRECTION DEPENDENCE OF THE CDW GAP

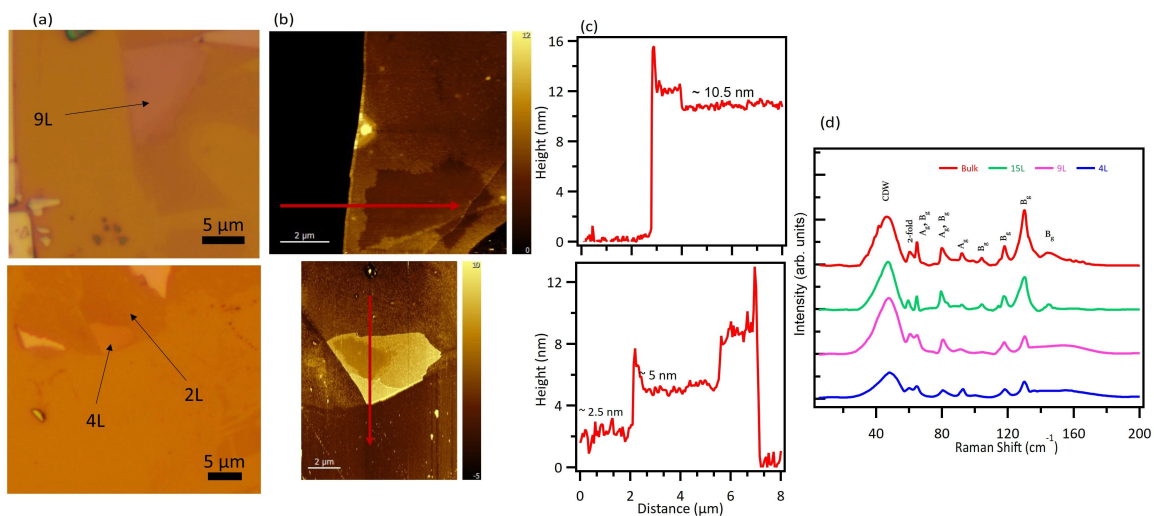
In Supplementary Figure 7, we present the dispersion maps, integrated EDCs and the Fermi fits of the leading edge for cut directions $\bar{\Gamma} - \tilde{A}$ through $\bar{\Gamma} - \tilde{D}$ as defined in Main text Figure 4. A clear signature of gap decreasing as the direction moves from $\bar{\Gamma} - \tilde{A}$ towards $\bar{\Gamma} - \tilde{D}$ can be observed. The results of the measurement taken at a temperature of 15 K do not show significant differences (see Supplementary Figure 8).

Supplementary References

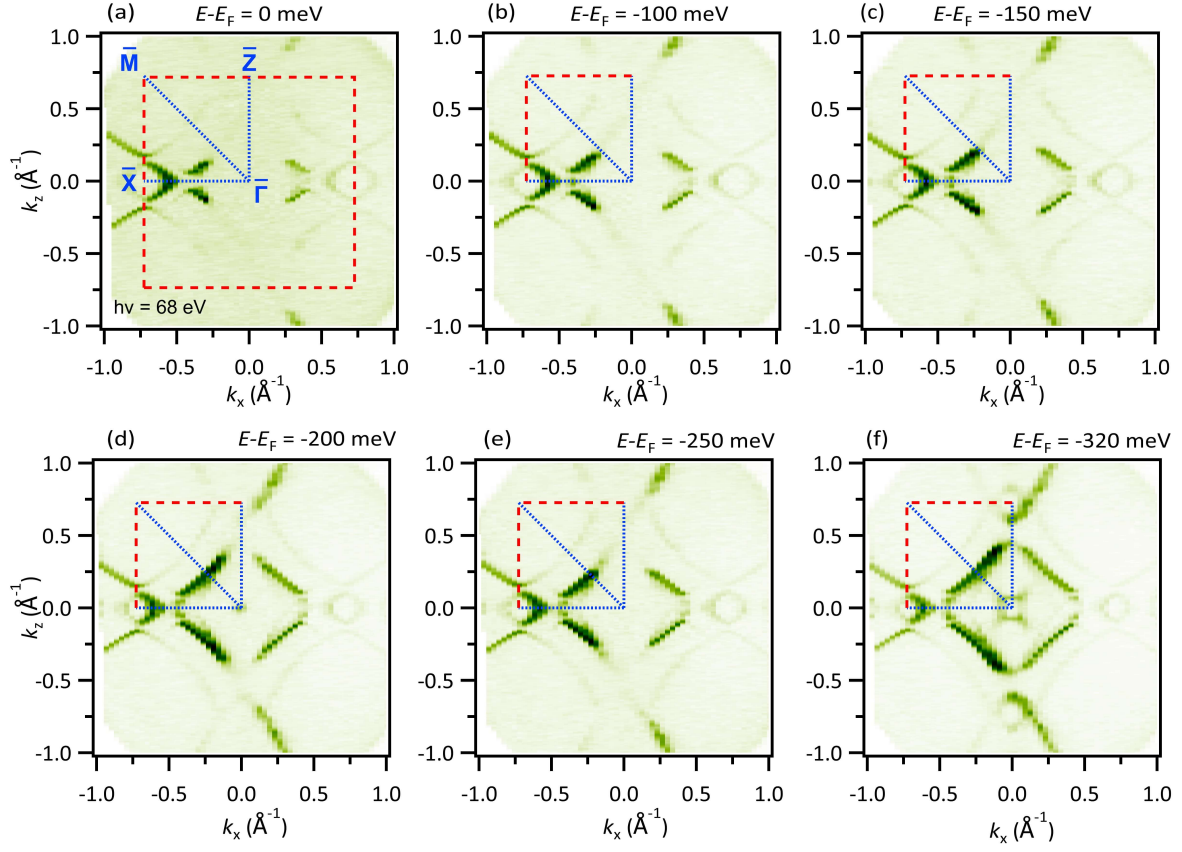
- [1] Yumigeta, K. et al. Advances in Rare-Earth Tritelluride Quantum Materials: Structure, Properties, and Synthesis. *Adv. Sci.* **8**, 2004762 (2021).
- [2] Chen, Y. et al. Raman spectra and dimensional effect on the charge density wave transition in GdTe₃. *Appl. Phys. Lett.* **115**, 151905 (2019).
- [3] Wang, Y. et al. Axial Higgs mode detected by quantum pathway interference in RTe₃. *Nature* **606**, 896 (2022).



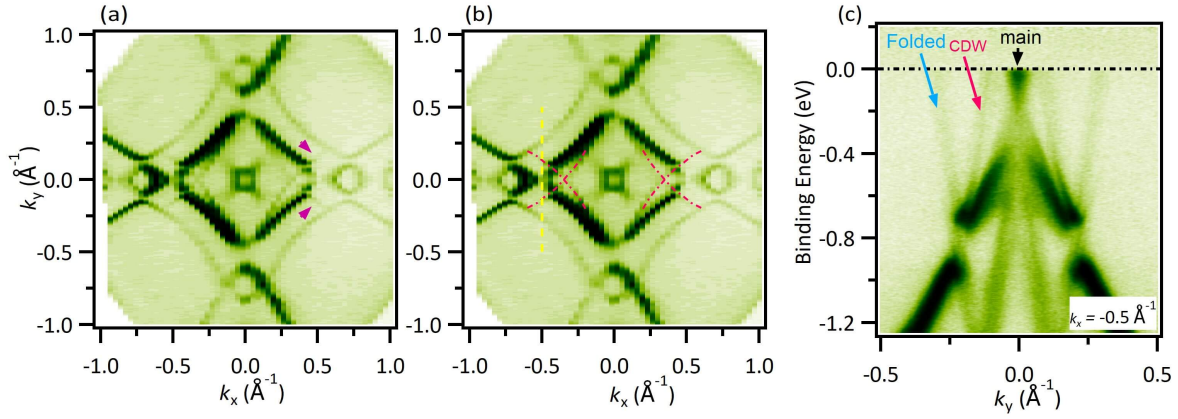
Supplementary Figure 1. **a** Microprobe analysis of the chemical composition of GdTe₃ single crystal. **b** Temperature variation of the specific heat over a wide range of temperature. Inset: the data collected in the vicinity of the CDW transition.



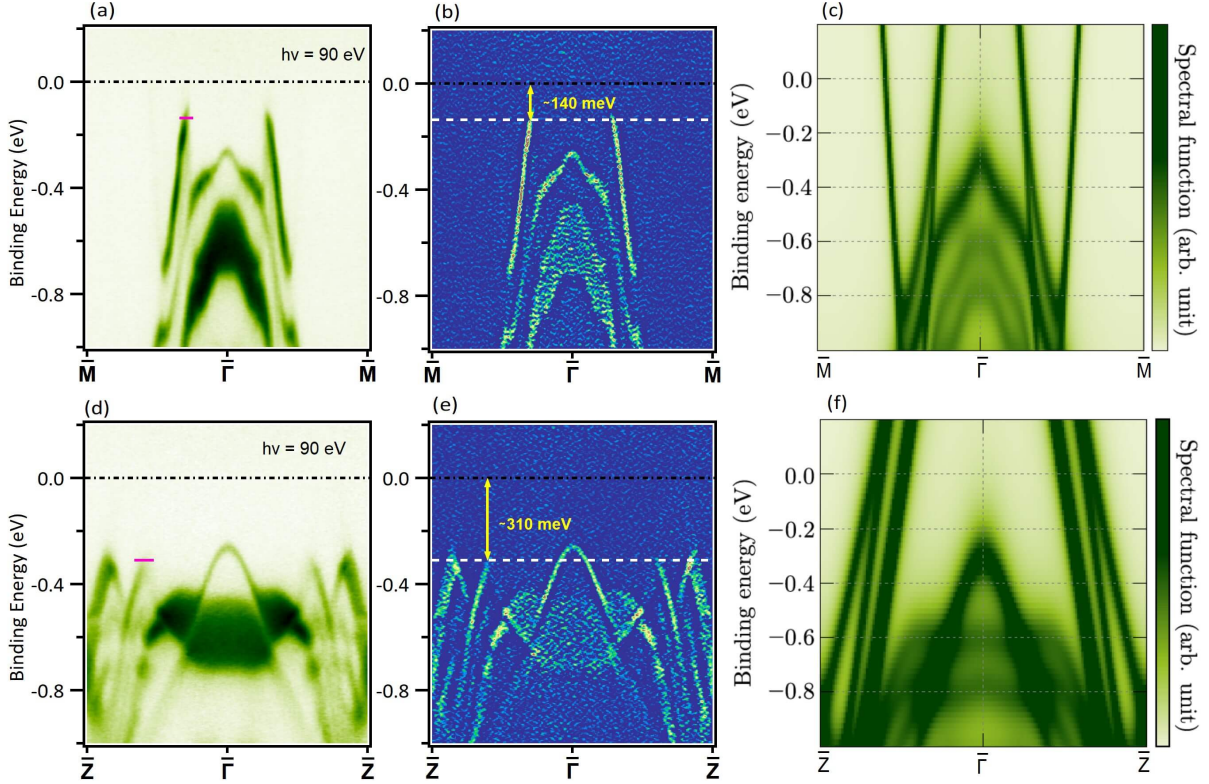
Supplementary Figure 2. Mechanical exfoliation of GdTe₃ flakes and Raman spectroscopy results. **a** Optical image, **b** AFM image, and **c** height profiles of GdTe₃ flakes exfoliated from bulk crystals. **d** Raman spectroscopy results on bulk and few layered samples indicated.



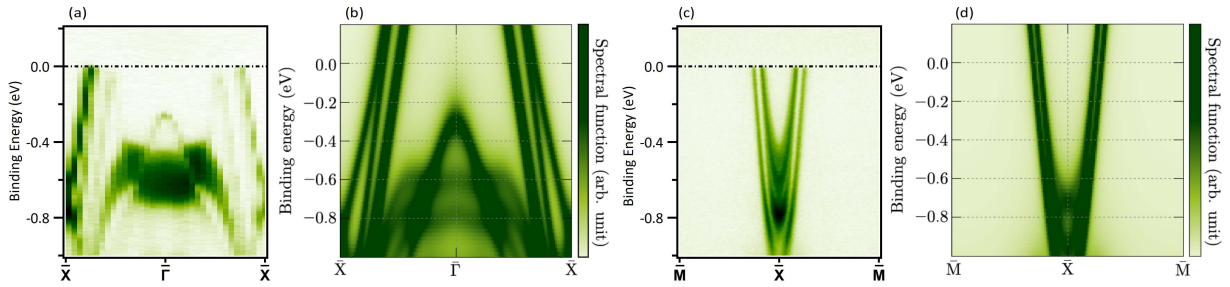
Supplementary Figure 3. Constant energy contours obtained for 68 eV photon energy at binding energies of **a** 0 meV (FS), **b** 100 meV , **c** 150 meV , **d** 200 meV , **e** 250 meV , and **f** 320 meV (experimental Brillouin zone in green and high-symmetry lines/points in cyan color). Data were collected at the SSRL beamline 5-2 at a temperature of 8 K .



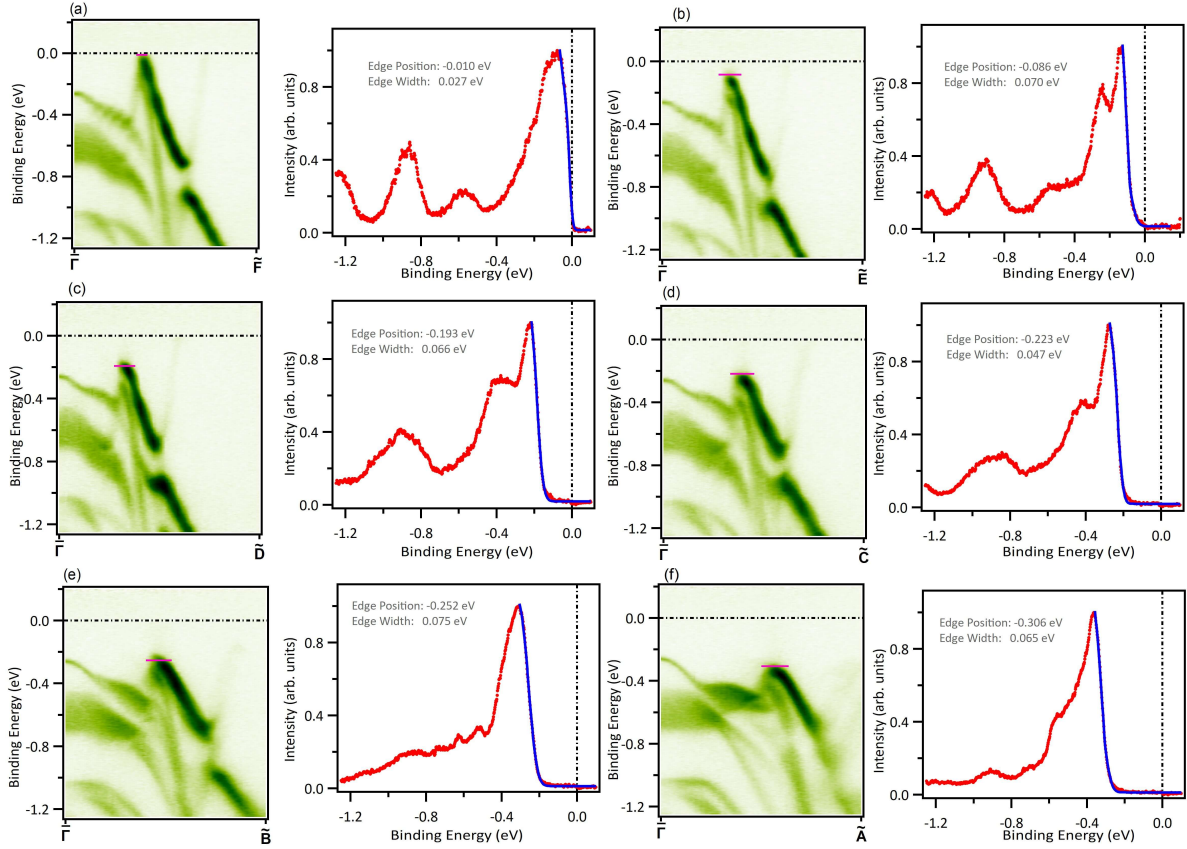
Supplementary Figure 4. Observation of CDW bands. **a** Energy contour integrated within a 50 meV window centered at 300 meV binding energy. **b** Same energy contour as in (a) with CDW induced features represented by magenta colored dashed curves. **c** Dispersion map taken for a $k_x = 0 \text{\AA}^{-1}$ cut represented by the yellow dashed line in (b).



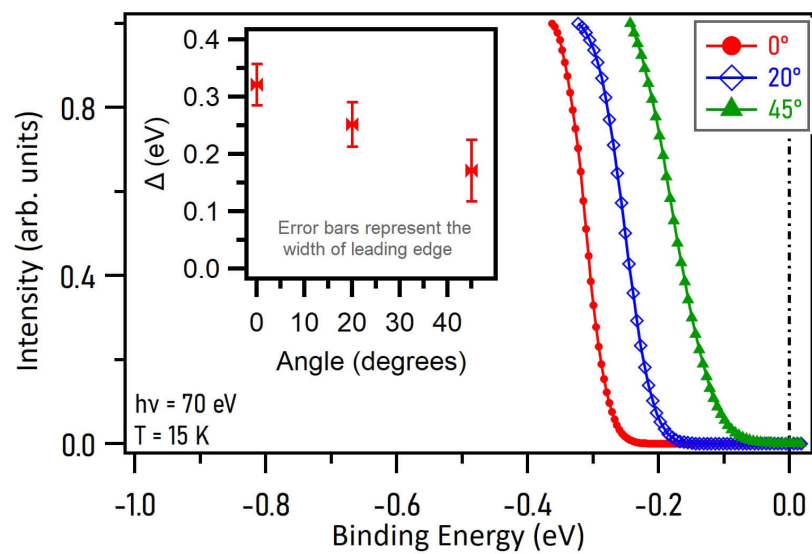
Supplementary Figure 5. Dispersion maps for 90 eV measurements. **a** Dispersion map and **b** its second derivative along $\bar{M} - \bar{\Gamma} - \bar{M}$. **c** Calculated surface spectrum along $\bar{M} - \bar{\Gamma} - \bar{M}$ without taking into account the CDW ordering. **d** Dispersion map and **e** its second derivative along $\bar{Z} - \bar{\Gamma} - \bar{Z}$. **f** Calculated surface spectrum along $\bar{Z} - \bar{\Gamma} - \bar{Z}$ without considering CDW order.



Supplementary Figure 6. Dispersion maps along $\bar{X} - \bar{\Gamma} - \bar{X}$ and $\bar{M} - \bar{X} - \bar{M}$. **a** Dispersion map along $\bar{X} - \bar{\Gamma} - \bar{X}$. **b** Calculated surface spectrum ($\bar{X} - \bar{\Gamma} - \bar{X}$) projection on the (010) surface. **c** Dispersion map along $\bar{M} - \bar{X} - \bar{M}$. **d** Calculated surface spectrum along $\bar{M} - \bar{X} - \bar{M}$ projected on the (010) surface.



Supplementary Figure 7. Direction dependent gap. Dispersion maps (left panel) and the energy distribution curves integrated within the momentum window indicated by the magenta lines in the dispersion maps (right panel) along **a** $\bar{\Gamma} - \tilde{F}$, **b** $\bar{\Gamma} - \tilde{E}$, **c** $\bar{\Gamma} - \tilde{D}$, and **d** $\bar{\Gamma} - \tilde{C}$, **e** $\bar{\Gamma} - \tilde{B}$, **f** $\bar{\Gamma} - \tilde{A}$. These directions represent the cuts at an angle of respectively: 62° , 55° , 40° , 30° , 20° , and 10° , from the $\bar{\Gamma} - \bar{Z}$ direction. The leading edges have been fitted by Fermi edge fitting.



Supplementary Figure 8. Fitted leading edges (normalized) for the angles noted in the plot. Inset: Gap size below the Fermi level, where the error bars represent the width of the leading edge. Data were taken at the ALS beamline 10.0.1.2 at a temperature of 15 K.